ACS APPLIED NANO MATERIALS

Article

Cite This: *ACS Appl. Nano Mater.* 2018, 1, 989−996

www.acsanm.org

Obtaining Structural Parameters from STEM−EDX Maps of Core/Shell Nanocrystals for Optoelectronics

Jacob T. Held,[†] Katharine I. Hunter,[‡] Nabeel Dahod,[§] Benjamin Greenberg,[‡] Danielle Reifsnyder Hickey,[†] William A. Tisdale,[§] Uwe Kortshagen,[‡] and K. Andre Mkhoyan*,[†]

[†]Department of Chemical Engineering and Materials Science and [‡]Department of Mechanical Engineering, University of Minnesota, Minneapolis, Minnesota 55455, United States

[§]Department of Chemical Engineering, Massachusetts Institute of Technology, Cambridge, Massachusetts 02139, United States

Supporting Information

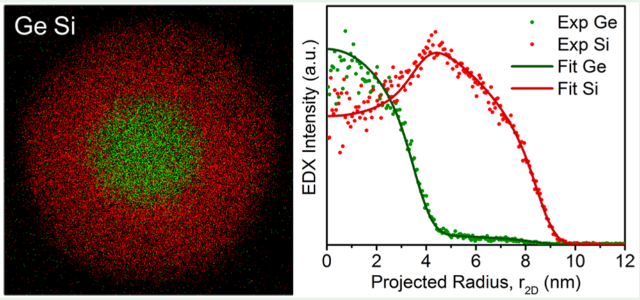

ABSTRACT: Characterization efforts of core/shell and core/multishell nanocrystals have struggled to quantitatively evaluate the interface width between the core and shell materials despite its importance in their optoelectronic properties. Here, we demonstrate a scanning transmission electron microscopy (STEM) method for measuring the radial elemental composition of two spherical core/shell nanocrystal systems, Ge/Si core/shell and CdSe/CdS/ZnS core/double-shell nanocrystals. By fitting model-based radial distributions of elements to measured STEM−energy-dispersive X-ray (EDX) maps, this method yields reliable and accurate measurements of interface broadening as well as core and shell sizes, surface roughness, and the fraction of core material in the shell. The direct evaluation of the structural parameters is an important step toward improving the synthesis of core/shell nanocrystals and optimizing their optoelectronic properties.

KEYWORDS: *core, shell, nanocrystal, interface, STEM, EDX, characterization*

INTRODUCTION

Semiconductor nanocrystals (NCs) exhibit many interesting and useful size-dependent optoelectronic properties[1,2] and have gained increasing applications in fields ranging from optical displays[3,4] to biological imaging.[5−7] They are often covered with shells to protect them from oxidation and surface trap states[8−10] and to better control the optoelectronic[11−14] and catalytic[15,16] properties through induced strain and band alignment between the core and shell. The properties of these core/shell NCs can be further tuned by controlling the core and shell shape, size, and composition.[17−19] In addition to these parameters, the sharpness of the interface between the core and shell also affects the properties of the NCs.[20−25] Therefore, it is important to reliably measure and modify this interface. However, measuring the width of the core/shell interface remains a major challenge in the characterization of these NCs.

Raman spectroscopy has been used to detect interfacial mixing in core/shell nanostructures,[26−28] but it is not applicable for all core/shell NCs and only yields ensemble-average values from relatively large quantities of NCs. Scanning transmission electron microscopy (STEM) combined with energy-dispersive X-ray (EDX) spectroscopy or electron energy-loss spectroscopy, on the other hand, presents the unique opportunity to analyze individual NCs at the atomic scale with a wide variety of elemental compositions.[14,29−31] It should be noted that tomography in transmission electron microscopy (TEM) can also achieve atomically accurate reconstructions of some NCs.[32−34] However, this approach is inapplicable when the difference between the atomic numbers (ΔZ) of the elements in the core and shell is small, which is common in core/shell NCs.

Earlier reports demonstrated that, despite limitations due to electron beam damage, reliable STEM−EDX maps and line profiles can be obtained from individual core/shell NCs, showing their core/shell structure.[31,35] Some attempts to obtain elemental distributions from nanomaterials using STEM−EDX have also been made.[36−38] However, these studies do not provide a method for the systematic and quantitative determination of structural information from core/shell NCs that is applicable to a wide variety of elemental compositions and is capable of accurately evaluating the core/shell interface width of individual NCs.

In this study, we show that, given a well-defined (in this case, spherical) NC geometry, it is possible to quantify with high certainty the radial elemental composition of a core/shell NC from a single STEM−EDX map and, most importantly, to estimate the sharpness of the interface between the core and

Received: December 27, 2017
Accepted: January 11, 2018
Published: January 11, 2018

DOI: 10.1021/acsanm.7b00398

shell. We demonstrate a quantitative analysis of the elemental distribution by fitting a model to STEM−EDX maps of the NCs. The analysis is first performed on plasma-grown Ge/Si core/shell NCs.[14] Then, we demonstrate the practical application of this analysis to widely studied CdSe/CdS/ZnS core/double-shell NCs.[8,24,39]

METHODS

Synthesis of Ge/Si Core/Shell NCs. The details of the process of producing Ge/Si core/shell NCs from a capacitively coupled nonthermal plasma were described previously.[14] In brief, this core/shell NC growth was achieved in a single flow-through plasma reactor by first injecting the core precursor and, after its depletion, injecting the shell precursor further downstream. An argon plasma was generated by the application of 50 W forward power at 13.56 MHz to a pair of copper electrodes encircling a 1-in.-o.d. glass tube. The primary gas feed, consisting of argon (20 sccm), dihydrogen (25 sccm), and $GeCl_4$ vapor (50 mTorr partial pressure), entered the reactor upstream of the plasma. Within the plasma, germanium (Ge) NCs nucleate and grow until the $GeCl_4$ precursor is depleted. Further downstream, the secondary gas feed, consisting of SiH_4 (0.2 sccm) diluted in argon (9.8 sccm), was injected into the plasma through a stainless steel toroidal inlet with 16 evenly spaced 1 mm holes around the circumference of the reactor tube. Within the plasma, SiH_4 decomposes and grows as an epitaxial silicon (Si) shell onto the Ge cores. The total pressure in the reactor chamber was held constant at 2 Torr by an orifice placed downstream of the plasma. NCs were deposited directly onto thin carbon with holey support TEM grids by acceleration through this orifice and impaction onto the grid.

Synthesis of CdSe/CdS/ZnS Core/Shell/Shell NCs. CdSe cores were prepared via modification of a previously reported method.[40] The synthesis was conducted in a nitrogen environment through the use of an air-free Schlenk line. First, cadmium oxide (80 mg) was combined with stabilizing organic ligands, tri-*n*-octylphosphine oxide (TOPO; 6 g) and octadecylphosphonic acid (562 mg), and degassed at 120 °C. The resulting solution was then heated to 300 C under nitrogen and left until it became clear (approximately 2 h). The temperature was ramped to 320 °C, and tri-*n*-octylphosphine (TOP; 1.5 mL) was injected to replenish the noncoordinated ligand in solution. The temperature was then ramped to the growth temperature (355 °C), and a solution of selenium (Se) coordinated with TOP was swiftly injected to create the nucleation burst that initiates NC growth. NCs were purified via precipitation, first by the addition of acetone to remove excess TOPO and then by the addition of a 2:1 methanol/butanol solution to precipitate the NCs. The final product was redispersed in an organic solvent and stored in a nitrogen glovebox.

The epitaxial growth of CdS and ZnS capping shells on previously prepared CdSe NCs proceeded via modification of the protocol published by Boldt et al.[24] Stock solutions of zinc oleate and cadmium oleate were prepared as outlined in that protocol. Briefly, in a nitrogen environment (via Schlenk line), a dispersion of previously prepared CdSe NCs (100 nmol) was dissolved in a coordinating organic solvent [3 mL of oleylamine and 3 mL of octadecene (ODE)], and the temperature was raised to 310 °C. When the temperature reached 280 °C, cadmiums (cadmium oleate) and sulfur (octanethiol) precursors dissolved in ODE were added dropwise via a syringe pump. The quantity of the cadmium precursor was used to control the shell thickness and is calculated using the core size, desired thickness, and lattice constant of wurtzite CdS. A 1.5-fold excess of thiol was used, and the injection rate was varied such that one monolayer of CdS was grown per hour. After the injection was complete, the solution was maintained at 200 °C, while organic ligands were replenished via the dropwise injection of 1 mL of oleic acid. Lingering volatiles in the solution were pulled off via vacuum (30 min), and the temperature was then raised to 280 °C. When the temperature reached 240 °C, dropwise injection of the zinc (zinc oleate) and sulfur (octanethiol) precursors in ODE was started. The quantity of the precursor required and the rate of injection were determined as above for the CdS shell preparation. After the precursors were added, the reaction mixture was allowed to cool to room temperature. The CdSe/CdS/ZnS core/double-shell NCs were purified via precipitation by the addition of acetone until the solution became turbid. The precipitate was redispersed and purified at least three times, or until the resulting solution remained clear. Purified dispersions were stored in a nitrogen glovebox.

An aliquot of the CdSe/CdS/ZnS NC dispersion was diluted 10 times and drop-cast onto ultrathin carbon with holey support TEM grids. To protect the particles from beam damage during STEM−EDX map acquisition, the grids were then coated with Al_2O_3 by atomic layer deposition (ALD) using a Cambridge Nanotech/Ultratech Savannah S2000 reactor and via a procedure similar to that described by Thimsen et al.[41] First, the NCs were heated under a dinitrogen flow at 180 °C and 0.3 Torr for 30 min. Then, ∼4 nm Al_2O_3 coatings were deposited at 180 °C using 40 cycles of ALD. Sequentially, each cycle consisted of a 0.1 s trimethylaluminum (TMA) pulse, a 30 s dinitrogen purge, a 0.1 water pulse, and a 30 s dinitrogen purge. The maximum pressure was 3 Torr during TMA pulses and 400 Torr during water pulses, and the minimum pressure was 0.3 Torr during dinitrogen purges.

STEM−EDX Measurements. All NCs were analyzed using an aberration-corrected FEI-Titan G2 60-300 sanning tensmission electron microscope equipped with a Super-X energy-dispersive X-ray spectrometer located at the University of Minnesota.[42,43] STEM−EDX experiments were performed at 60 kV STEM beam voltage with a 25 mrad convergence angle, a 125 pA beam current, and a 68 mrad high-angle annular-dark-field (HAADF) detector inner angle. EDX spectral images were acquired with frame-by-frame drift correction through the Bruker *ESPRIT 1.9* software with a dwell time of 3 μs/pixel and a pixel resolution of 0.04 nm/pixel for the Si/Ge sample and 0.06 nm/pixel for the CdSe/CdS/ZnS sample. For the Si/Ge sample, the Si and Ge K-edges were background-subtracted and integrated, producing the spectral images. In the CdSe/CdS/ZnS NC sample, the S K-edge and Se, Cd, and Zn L-edges were used.

RESULTS AND DISCUSSION

The Ge/Si NCs used in this study were predominantly spherical in shape. Therefore, a spherical, concentric, core/shell NC model was used as the basis for the simulations. Taking advantage of this symmetry, the distributions of elements within the NCs were expressed as one-dimensional (1D) functions of the spherical radius that were integrated along the z axis to produce 1D projected distributions of elements. Likewise, the experimental two-dimensional (2D) STEM−EDX maps were converted into 1D intensity profiles by radially averaging the EDX counts for each element around the center of the particle, as illustrated in Figure 1, allowing a direct comparison between the experimental data and simulated distributions.

Spherical radial concentration distributions were constructed using error functions to approximate core/shell interface broadening. This functional form was chosen because the solution to a spherically symmetrical interdiffusion model between a core and shell converges to these equations when little diffusion has occurred. This approximation also has the advantages of yielding intuitive results in the form of a standard deviation of each distribution and of being computationally inexpensive relative to the diffusion model. The similarity of the diffusion model and error function approximation for the core/shell systems studied here is demonstrated in the Supporting Information (SI). By using only the error function model, no distinction is made between the “roughness” and “interdiffusion” of the core and shell species. At the scale of individual atoms, as discussed here, this distinction is physically unclear. The error function model was also used as an approximation for the surface roughness.

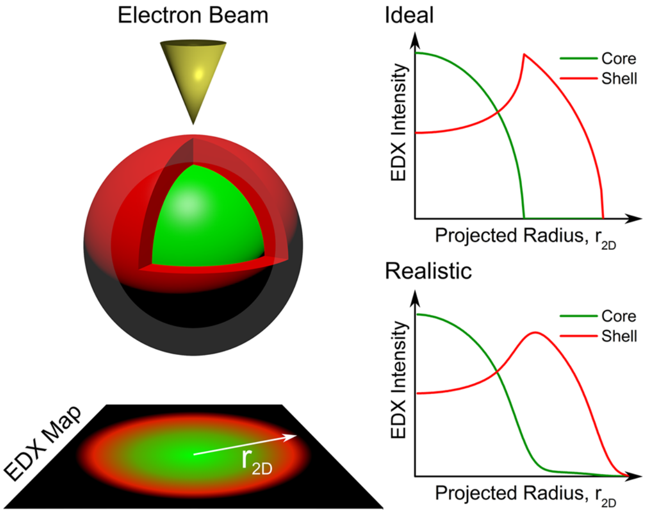

Figure 1. Schematic representation of the acquisition of an STEM–EDX map of a core/shell NC and radially averaged data from such a map. The (top) ideal case represents the radially averaged data of a perfectly spherical core and shell with a sharp interface and surface, mapped with a δ-functional probe. The (bottom) realistic case includes a diffuse interface and surface and a finite probe size.

When this approximation of the elemental distribution is applied to a simple core/shell system and the radius of the core is denoted as r_{core} and the width of the interface between the core and shell as σ_i (the standard deviation of the representative error function), the radial distribution of the core material A is expressed as

$$c_{\mathrm{A}}(r) = c_{\mathrm{core}}(r, r_{\mathrm{core}}, \sigma_{\mathrm{i}}) = \frac{1}{2}\left[1 - \mathrm{erf}\left(\frac{r_{\mathrm{core}} - r}{\sqrt{2}\,\sigma_{\mathrm{i}}}\right)\right] \tag{1}$$

Likewise, the radial distribution of the shell material B is expressed as

$$\begin{aligned} c_{\mathrm{B}}(r) &= c_{\mathrm{shell}}(r, r_{\mathrm{core}}, \sigma_{\mathrm{i}}, r_{\mathrm{shell}}, \sigma_{\mathrm{s}}) \\ &= \frac{1}{2}\left[1 - \mathrm{erf}\left(\frac{r_{\mathrm{shell}} - r}{\sqrt{2}\,\sigma_{\mathrm{s}}}\right)\right]\left[1 - c_{\mathrm{core}}(r, r_{\mathrm{core}}, \sigma_{\mathrm{i}})\right] \end{aligned} \tag{2}$$

where the outer radius of the shell is denoted as r_{shell} and the roughness of the outer surface of the shell as σ_{s}. This system of two coupled equations was then used to determine all four parameters describing the elemental distribution of the core/shell NC: the radii of the core and shell (r_{core} and r_{shell}) and the widths of the core/shell interface and the surface roughness (σ_{i} and σ_{s}). Before eqs 1 and 2 were applied as fitting functions to the experimental EDX data set to deduce these parameters, they were integrated along the STEM beam axis, z, to reflect the fact that experimental EDX maps are 2D projections of 3D NCs. Therefore, the two fitting functions are

$$f_{\mathrm{A}}(r_{2\mathrm{D}}) = \int_{-\infty}^{+\infty} c_{\mathrm{A}}(r)\,\mathrm{d}z \tag{3}$$

$$f_{\mathrm{B}}(r_{2\mathrm{D}}) = \int_{-\infty}^{+\infty} c_{\mathrm{B}}(r)\,\mathrm{d}z \tag{4}$$

The pair of functions (3) and (4) can, in principle, describe any STEM–EDX map obtained from spherical core/shell NCs with a nonsharp interface and surface, provided that little interdiffusion has occurred. However, in the systems studied here, NC synthesis introduced a nonnegligible concentration of the core material in the shells. To account for this, eqs 1 and 2 were modified to

$$c_{\mathrm{Ge}}(r) = c_{\mathrm{core}}(r, r_{\mathrm{core}}, \sigma_{\mathrm{i}}) + p c_{\mathrm{shell}}(r, r_{\mathrm{core}}, \sigma_{\mathrm{i}}, r_{\mathrm{shell}}, \sigma_{\mathrm{s}}) \tag{5}$$

$$c_{\mathrm{Si}}(r) = (1 - p) c_{\mathrm{shell}}(r, r_{\mathrm{core}}, \sigma_{\mathrm{i}}, r_{\mathrm{shell}}, \sigma_{\mathrm{s}}) \tag{6}$$

where p is the fraction of the residual core material, in this case Ge, in the Si shell.

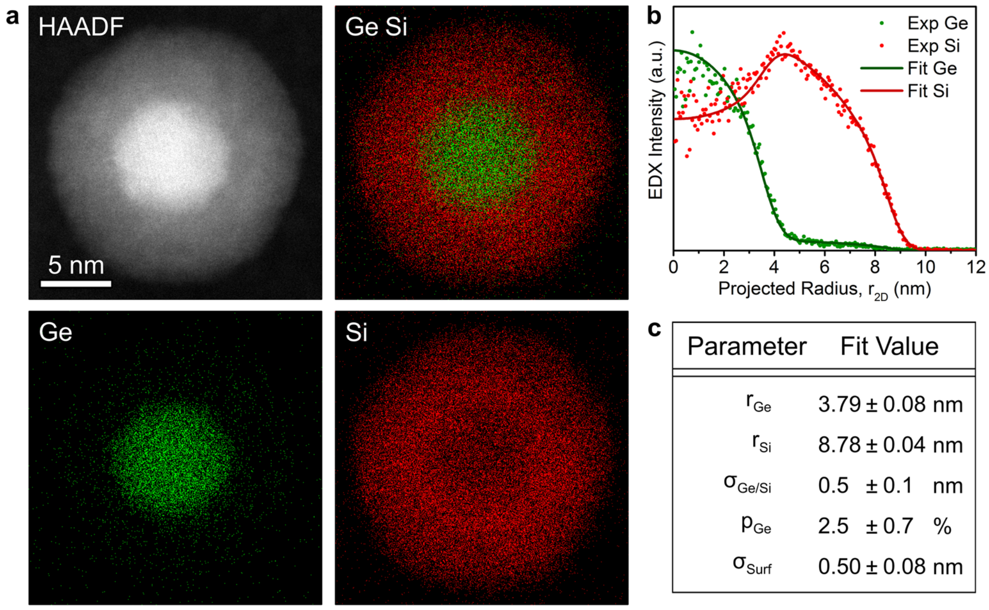

Parameter	Fit Value
r_{Ge}	3.79 ± 0.08 nm
r_{Si}	8.78 ± 0.04 nm
$\sigma_{\mathrm{Ge/Si}}$	0.5 ± 0.1 nm
p_{Ge}	2.5 ± 0.7 %
σ_{Surf}	0.50 ± 0.08 nm

Figure 2. Ge/Si core/shell NC analysis. (a) HAADF–STEM image and EDX maps of a Ge/Si core/shell NC. The HAADF image of the NC taken after EDX map acquisition shows Z contrast between the Ge core and Si shell. The composite EDX map of Ge (green) and Si (red) and individual EDX maps of Ge and Si demonstrate a clear differentiation between the core and shell material. (b) Radially averaged EDX data with corresponding fit, with core and shell signals scaled separately. (c) Parameters corresponding to the optimized fit.

DOI: 10.1021/acsanm.7b00398
ACS Appl. Nano Mater. 2018, 1, 989–996

The effects of the finite size of the STEM probe and its broadening should also be taken into consideration. In STEM, the probe that scans the sample has a finite size, defined by the convergence angle and voltage as well as the effective source size.[44,45] Scattering of the probe by atoms in the sample results in additional broadening as it propagates through the sample. Multislice-based simulations[46] of the experimental setup show that, with beam broadening included, the effective size of the STEM probe in this study was approximately 0.18 nm. Details of these simulations are presented in the SI. Therefore, the fitting functions (3) and (4) were convoluted with a Gaussian function with a full width at half-maximum of 0.18 nm to incorporate the effective size of the STEM probe before fitting to the EDX maps.

The fitting error was minimized using the Nelder–Mead method[47] to obtain all parameters describing the core and shell structure of the core/shell NCs: r_{core}, σ_i, r_{shell}, σ_s, and p. The fitting error was calculated as

$$\text{Er} = \frac{1}{N}\sum_{j=1}^{N}[r_{2\text{D}_j}(I_j^{\text{fit}} - I_j^{\text{exp}})]^2 \tag{7}$$

where N is the total number of data points in the intensity profiles and r_j, I_j^{fit}, and I_j^{exp} are the radius, fitted intensities, and experimental intensities, respectively. Here, the residual was multiplied by the 2D radius to account for the number of pixels encountered at each radius increasing proportionally to $2\pi r_{2\text{D}_j}$. This also accounts for the higher noise at low radii for radially averaged EDX data sets, which can be seen in Figures 2 and 4. After optimization of all parameters in each data set, the fitting uncertainty of each parameter was defined as the maximum change in the parameter that was necessary to increase the fitting error by 5%. The complete flowchart of this analysis can be found in the SI.

To prepare the experimental data for analysis, an ellipse was first fit to the STEM–EDX maps of each NC to determine the center and major/minor axis lengths and to ensure that the centers of the maps of each element were coincident (details of this analysis are provided in the SI). The average position of the fit centers was then set as the overall center of the NC, and each EDX map was radially averaged around this point. To maintain the spherical approximation of the NC geometry, NCs with an aspect ratio of 1.05 or greater were discarded, along with those with the centers for each element that varied by more than 0.4 nm, or 10 pixels. Data sets that met these criteria were further analyzed.

A uniform background of the Si EDX signal due to residual Si on the grids from NC synthesis was subtracted. The Si background was found by averaging the signal outside the NC for each EDX map. An example of this is shown in the SI. No significant Ge background was detected. Simulated projected distributions of the elements in spherical NCs were then fit to the radially averaged and background-subtracted experimental data sets. One example of the full analysis is presented in Figure 2.

The fitting procedure for the Ge/Si system resulted in a very good agreement between the experimental data and model, as shown in Figure 2. The radial distribution of the elements determined through this analysis is shown in Figure 3. The broadening at the core/shell interface as well as the surface roughness was determined to be 0.5 nm; this is comparable to the lattice parameter of the NC (0.56 nm), which was shown to be slightly strained by Hunter et al.[14] Because these values arise from a combination of interdiffusion at the interface, roughness, asymmetry, and nonconcentricity of the core/shell NCs, they represent the total contribution of these effects to the divergence from a perfect spherical core/shell system. In this case, the Ge core had an aspect ratio of 1.01 and the Si shell had an aspect ratio of 1.02, contributing 0.02 and 0.08 nm to the interface and surface roughness, respectively. Additionally, there was 0.2 nm offset between the core and shell centers, contributing 0.1 nm to the core/shell interface broadening measurement. No significant faceting was observed in the STEM images of the NCs studied here. The remaining interface and surface broadening widths (approximately 0.4 nm for the core/shell interface and 0.32 nm for the NC surface) arise from roughness/interdiffusion. Analyses of several other NCs are presented in the SI.

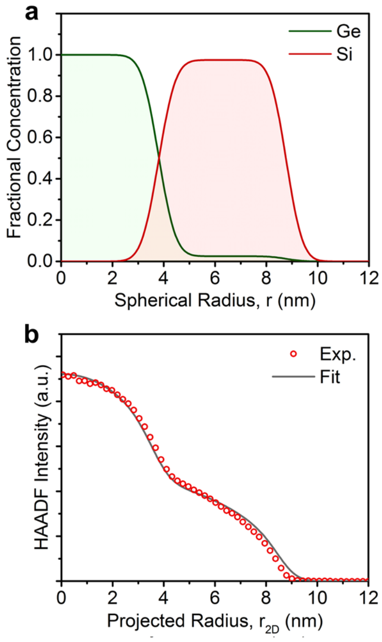

Figure 3. (a) Radial (spherical) distribution of Ge and Si within the NC shown in Figure 2, obtained from fitting. (b) HAADF image intensity profile fitted with a "*Z*-contrast" approximation using eq 8.

Additionally, analysis showed a uniform 2.5% Ge content in the Si shell. If this concentration of Ge in the shell were due to interdiffusion, it would be reflected in $\sigma_{\text{Ge/Si}}$, and there would be a significantly greater concentration of Si in the Ge core due to the much larger volume of the shell (approximately 10 times the core volume). It should also be noted that Ge K-edge X-rays (9.87 keV) are of higher energy than Si K-edge X-rays (1.74 keV), such that this Ge signal could not be produced via secondary fluorescence. While the opposite could happen (producing Si EDX counts), this interaction is extremely improbable because of the small size of the NCs (~10 nm) relative to the attenuation length (~120 μm).[48] The addition of another parameter to account for the shell material in the core fit was less than 0.5% and did not result in a significantly better fit. Therefore, we conclude that there was residual Ge precursor in the plasma at the point of Si precursor injection during the NC synthesis.[14]

Aside from some surface alterations, little change in the radially averaged HAADF profiles obtained before and after EDX acquisition was observed, demonstrating that minimal beam damage occurred during the experiment (for details, see the SI). While most core/shell NC systems exhibit little

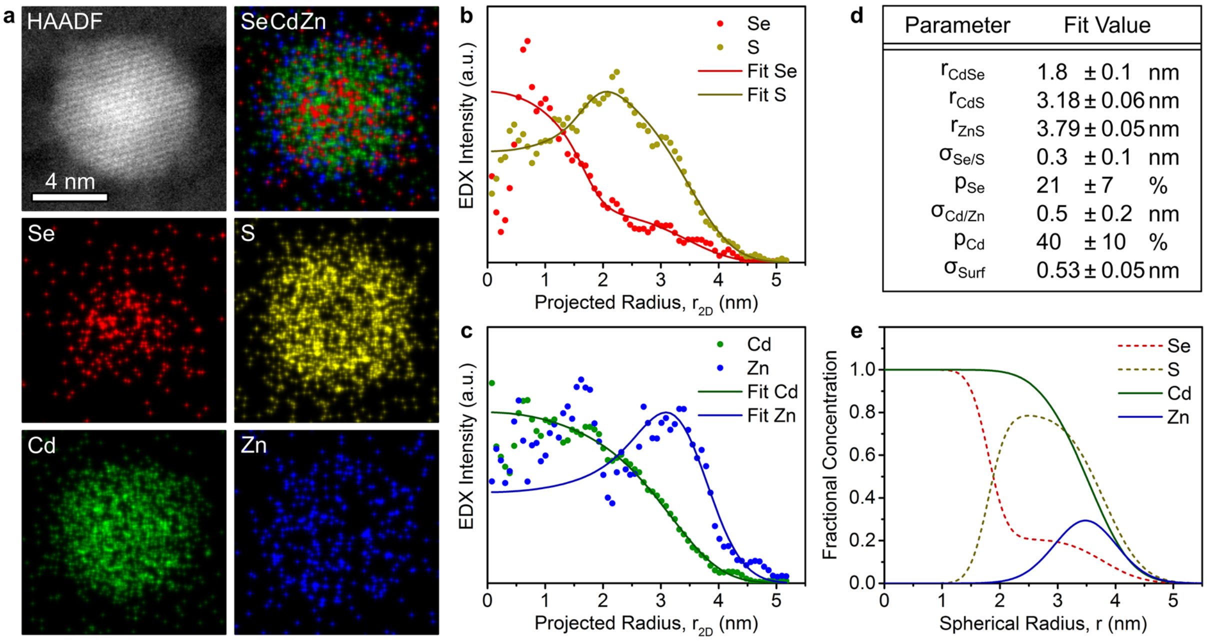

Parameter	Fit Value
r_{CdSe}	1.8 ± 0.1 nm
r_{CdS}	3.18 ± 0.06 nm
r_{ZnS}	3.79 ± 0.05 nm
$\sigma_{Se/S}$	0.3 ± 0.1 nm
p_{Se}	21 ± 7 %
$\sigma_{Cd/Zn}$	0.5 ± 0.2 nm
p_{Cd}	40 ± 10 %
σ_{Surf}	0.53 ± 0.05 nm

Figure 4. Application of the fitting procedure to a CdSe/CdS/ZnS core/double-shell NC. (a) HAADF−STEM image and EDX maps of a CdSe/CdS/ZnS core/double-shell NC. A three-pixel Gaussian blur has been applied to all EDX maps for visual clarity. (b and c) Radially averaged EDX data for the anion (Se/S) and cation (Cd/Zn) distributions and corresponding fits, scaled separately. (d) Parameters corresponding to the optimized fit. (e) Radial (spherical) distribution of each element within the NC, obtained from the fitting.

contrast between the core and shell materials, the large difference in the atomic number, and therefore contrast between Ge and Si, offered a unique opportunity to test the results from EDX analysis against HAADF−STEM images of the same particles. Therefore, for further confirmation of the model, the obtained projected distributions of the elements were fit to the HAADF signal according to

$$I^{\mathrm{ADF}}(r_{2\mathrm{D}}) = A[f_{\mathrm{Ge}}(r_{2\mathrm{D}})\, Z_{\mathrm{Ge}}{}^{\alpha} + f_{\mathrm{Si}}(r_{2\mathrm{D}})\, Z_{\mathrm{Si}}{}^{\alpha}] \qquad (8)$$

where $f_{\mathrm{Ge}}(r_{2\mathrm{D}})$ and $f_{\mathrm{Si}}(r_{2\mathrm{D}})$ are the projected radial distributions of Ge and Si (eqs 3 and 4), respectively, determined by fitting to EDX maps. Z_{Ge} and Z_{Si} are the atomic numbers of Ge and Si, and A and α are the fitting parameters. The parameter A provides scaling for the experimental ADF intensity, and its value is not meaningful for this analysis. The best fit corresponded to $\alpha = 1.4$, which lies within the range of quantitative STEM models for Z contrast in HAADF−STEM imaging (1.2−1.8)[49−51] and matches well with the more accurate prediction of 1.5 ± 0.1 by Wang et al.[51] for the experimental parameters used here. The result of this analysis is shown in Figure 3. It should be noted that, in principle, full analysis could be performed using only the HAADF−STEM data, such as that shown in Figure 3, but the fitting procedure would still require all five of the fitting parameters tabulated in Figure 2, plus α from eq 8. The reliability of such a six-parameter fit to a single data set (as opposed to five parameters split between two EDX map data sets) would be questionable. Additionally, the nontrivial background contrast from the carbon support, carbon contamination, and presence of ligands or ALD coating would complicate HAADF analysis even further. HAADF−STEM analysis also requires prior knowledge of the elemental composition, which is implicitly determined by EDX mapping.

In addition to the added complexity of a second shell, the CdSe/CdS/ZnS core/double-shell NCs studied here were significantly smaller and more beam-sensitive than the Ge/Si NCs. Because of residual ligands from the synthesis procedure, carbon contamination via oligomerization of loose ligands under the STEM beam also posed a challenge to STEM−EDX analysis. When the crystals already deposited on the TEM grids were coated with alumina via ALD to a thickness of 4 nm (40 deposition cycles), most of the experimental challenges were mitigated; the ligands were driven off during ALD, and the alumina coating protected the crystals during analysis. It should be noted that thinner ALD coatings of only 3−4 deposition cycles also reduced carbon contamination while leaving a more even background for imaging. However, these thin coatings did little to protect the NCs, which damaged rapidly under the STEM beam.

During EDX map acquisition, the alumina film suffered some beam damage, contributing a significant textured background to the HAADF images. While the major sources of contrast in the image remained stationary, allowing reliable drift correction during acquisition, the damaged alumina film made it impractical to quantitatively compare the before/after HAADF images of the NCs in the same way as the Ge/Si system. However, the underlying NC sustained minimal damage during the EDX map acquisition based on the consistent shape, dimensions, and lattice features of the underlying NC observed in the before/after HAADF images (see the SI).

The same radial-averaging preparation procedure as that described for the Ge/Si NCs was applied to the EDX maps of the CdSe/CdS/ZnS NCs. Here, the sulfur (S) and cadmium (Cd) maps were used to determine the center of the NC because they provided the highest total counts of the elements in this system, and therefore the best signal-to-noise ratio.

The core/double-shell CdSe/CdS/ZnS NC was modeled as two coupled core/shell distributions: one representing the anionic Se/S core/shell and the other representing the cationic Cd/Zn core/shell, with the surface radius and roughness shared between the two distributions. A schematic diagram of this treatment is provided in the SI. Thus, this model required four coupled elemental distribution equations, one representing each element, and three more parameters than the Ge/Si core/shell NC: the dimensions and broadening of the additional interface and the concentration of the core material in the second shell. One example of this analysis is presented in Figure 4.

The results of this analysis indicated a relatively sharp (0.3 nm) CdSe/CdS interface and a slightly broader (0.5 nm) CdS/ZnS interface. The outer surface roughness was 0.5 nm. Because the thickness of the ZnS shell was only 0.6 nm, the broadening of the CdS/ZnS interface and the outer surface roughness overlap over the majority of the ZnS shell, as is shown in Figure 4e. In this sample, there was a large concentration of the core material in the outer shells, with the S shell composed of about 20% Se and the Zn shell containing about 40% Cd. We believe that this is due to solvation and redeposition of the material during shell growth as well as the presence of unreacted cadmium oleate during the addition of the ZnS shell.

Because these NCs were smaller and yielded fewer total EDX counts from each element before nonnegligible damage was observed, the uncertainties in each fit parameter were percentagewise larger than those in the Ge/Si sample analysis but still represent only a fraction of the crystal unit cell (for example, a_{CdS} = 0.416 nm), which, from a structural characterization point of view, is quite good. The significant noise and poorer fits observed in the Se and Zn EDX data below 1−2 nm radii arise from the low number of EDX counts for these elements. However, EDX data from the complementary elements (S and Cd), which are present in higher concentrations in the NCs, are less noisy. Because each of the fit curves represents the optimized fit of the pair of elements, this provides extra fitting stability even when some elements have relatively noisy EDX data sets. Despite the complexity of the double-shell system and the practical limitations of data acquisition, the method, nonetheless, yields quantitative results for the size and broadening of both core/shell interfaces.

CONCLUSIONS

In this study, we demonstrated a model-based fitting method for the quantitative compositional analysis of STEM−EDX maps of spherical core/shell NCs. Simulated projected radial distributions of the elements were fit to the corresponding EDX intensity profiles, yielding values for the core and shell sizes, interface broadening, surface roughness, and fraction of core material in the shell. The method was demonstrated for two spherical NC systems: simpler Ge/Si core/shell and more complex CdSe/CdS/ZnS core/double-shell NCs. The method allows an evaluation of the interface widths with precision as high as 0.1−0.2 nm.

Although this analysis was limited to spherical core/shell NCs, it could be expanded to more complex NC geometries by analyzing the full 2D maps rather than radially averaging the data into one dimension. Such a procedure would increase the number of simultaneous fitting parameters. Therefore, a better signal-to-noise ratio in the EDX maps would be required to maintain the same certainty in the fit.

This method is readily applicable to a wide variety of elemental compositions of core/shell NCs, provided that each element exhibits resolvable EDX spectral features. Additionally, it relies on the relative EDX intensities rather than the absolute intensities and therefore does not require detector calibration to EDX standards. Finally, it provides important local information specific to an individual NC but could be readily automated to quantify the properties of numerous core/shell NCs for improved statistical analysis of a sample of NCs. Given the influence of the interface broadening, composition, and surface structure on the optoelectronic properties of core/shell NCs and the current lack of tools to evaluate these parameters, this characterization approach may serve as an important step in optimizing the synthesis of core/shell systems for use in optoelectronic devices.

ASSOCIATED CONTENT

Supporting Information

The Supporting Information is available free of charge on the ACS Publications website at DOI: 10.1021/acsanm.7b00398.

> Evaluation of a diffusion-based model, details on probe broadening, flowchart for the analysis procedure, details on center determination and background subtraction, supplemental data sets and analyses, evaluation of electron beam damage, and schematic description of the core/double-shell analysis approach (PDF)

AUTHOR INFORMATION

Corresponding Author

*E-mail: mkhoyan@umn.edu. Tel: 612-625-2059. Fax: 612-626-7246.

ORCID

Jacob T. Held: 0000-0003-3864-4314
Katharine I. Hunter: 0000-0001-8639-5012
Benjamin Greenberg: 0000-0002-5013-5996
William A. Tisdale: 0000-0002-6615-5342
K. Andre Mkhoyan: 0000-0003-3568-5452

Notes

The authors declare no competing financial interest.

ACKNOWLEDGMENTS

This project was supported by the MRSEC program of the National Science Foundation under Award DMR-1420013. STEM analysis was performed in the College of Science and Engineering Characterization Facility of the University of Minnesota, which receives partial support from the NSF through the MRSEC program. N.D. and W.A.T. were supported by the Division of Chemistry and Division of Materials Research, U.S. National Science Foundation, under Award 1452857. D.R.H. was supported by C-SPIN, one of six centers of STARnet, a Semiconductor Research Corporation program, sponsored by MARCO and DARPA.

REFERENCES

(1) Norris, D. J.; Bawendi, M. G. Measurement and Assignment of the Size-Dependent Optical Spectrum in CdSe Quantum Dots. *Phys. Rev. B: Condens. Matter Mater. Phys.* **1996**, *53* (24), 16338−16346.

(2) Mangolini, L. Synthesis, Properties, and Applications of Silicon Nanocrystals. *J. Vac. Sci. Technol., B: Nanotechnol. Microelectron.: Mater., Process., Meas., Phenom.* **2013**, *31* (2), 20801.

(3) Bourzac, K. Quantum Dots Go on Display. *Nature* **2013**, *493* (7432), 283−283.

(4) Shirasaki, Y.; Supran, G. J.; Bawendi, M. G.; Bulović, V. Emergence of Colloidal Quantum-Dot Light-Emitting Technologies. *Nat. Photonics* **2013**, *7* (1), 13−23.

(5) Bruchez, M., Jr.; Moronne, M.; Gin, P.; Weiss, S.; Alivisatos, A. P. Semiconductor Nanocrystals as Fluorescent Biological Labels. *Science* **1998**, *281* (5385), 2013−2016.

(6) Medintz, I. L.; Uyeda, H. T.; Goldman, E. R.; Mattoussi, H. Quantum Dot Bioconjugates for Imaging, Labelling and Sensing. *Nat. Mater.* **2005**, *4* (6), 435−446.

(7) Michalet, X.; Pinaud, F. F.; Bentolila, L. A.; Tsay, J. M.; Doose, S.; Li, J. J.; Sundaresan, G.; Wu, A. M.; Gambhir, S. S.; Weiss, S. Quantum Dots for Live Cells, in Vivo Imaging, and Diagnostics. *Science (Washington, DC, U. S.)* **2005**, *307* (5709), 538−544.

(8) Pust, P.; Schmidt, P. J.; Schnick, W. A Revolution in Lighting. *Nat. Mater.* **2015**, *14* (5), 454−458.

(9) Wang, F.; Liu, X. Recent Advances in the Chemistry of Lanthanide-Doped Upconversion Nanocrystals. *Chem. Soc. Rev.* **2009**, *38* (4), 976−989.

(10) Schärtl, W. Current Directions in Core-Shell Nanoparticle Design. *Nanoscale* **2010**, *2* (6), 829−843.

(11) Balet, L. P.; Ivanov, S. A.; Piryatinski, A.; Achermann, M.; Klimov, V. I. Inverted Core/Shell Nanocrystals Continuously Tunable between Type-I and Type-II Localization Regimes. *Nano Lett.* **2004**, *4* (8), 1485−1488.

(12) Reiss, P.; Protière, M.; Li, L. Core/Shell Semiconductor Nanocrystals. *Small* **2009**, *5* (2), 154−168.

(13) Smith, A. M.; Mohs, A. M.; Nie, S. Tuning the Optical and Electronic Properties of Colloidal Nanocrystals by Lattice Strain. *Nat. Nanotechnol.* **2009**, *4* (1), 56−63.

(14) Hunter, K. I.; Held, J. T.; Mkhoyan, K. A.; Kortshagen, U. R. Nonthermal Plasma Synthesis of Core/Shell Quantum Dots: Strained Ge/Si Nanocrystals. *ACS Appl. Mater. Interfaces* **2017**, *9* (9), 8263−8270.

(15) Strasser, P.; Koh, S.; Anniyev, T.; Greeley, J.; More, K.; Yu, C.; Liu, Z.; Kaya, S.; Nordlund, D.; Ogasawara, H.; Toney, M. F.; Nilsson, A. Lattice-Strain Control of the Activity in Dealloyed Core-Shell Fuel Cell Catalysts. *Nat. Chem.* **2010**, *2* (6), 454−460.

(16) Sasaki, K.; Wang, J. X.; Naohara, H.; Marinkovic, N.; More, K.; Inada, H.; Adzic, R. R. Recent Advances in Platinum Monolayer Electrocatalysts for Oxygen Reduction Reaction: Scale-up Synthesis, Structure and Activity of Pt Shells on Pd Cores. *Electrochim. Acta* **2010**, *55* (8), 2645−2652.

(17) Chen, W.-T.; Yang, T.-T.; Hsu, Y.-J. Au-CdS Core−Shell Nanocrystals with Controllable Shell Thickness and Photoinduced Charge Separation Property. *Chem. Mater.* **2008**, *20* (23), 7204−7206.

(18) Ghosh Chaudhuri, R.; Paria, S. Core/Shell Nanoparticles: Classes, Properties, Synthesis Mechanisms, Characterization, and Applications. *Chem. Rev.* **2012**, *112* (4), 2373−2433.

(19) Zhang, F.; Che, R.; Li, X.; Yao, C.; Yang, J.; Shen, D.; Hu, P.; Li, W.; Zhao, D. Direct Imaging the Upconversion Nanocrystal Core/Shell Structure at the Subnanometer Level: Shell Thickness Dependence in Upconverting Optical Properties. *Nano Lett.* **2012**, *12* (6), 2852−2858.

(20) McBride, J.; Treadway, J.; Feldman, L. C.; Pennycook, S. J.; Rosenthal, S. J. Structural Basis for Near Unity Quantum Yield Core/Shell Nanostructures. *Nano Lett.* **2006**, *6* (7), 1496−1501.

(21) Cragg, G. E.; Efros, A. L. Suppression of Auger Processes in Confined Structures. *Nano Lett.* **2010**, *10* (1), 313−317.

(22) García-Santamaría, F.; Brovelli, S.; Viswanatha, R.; Hollingsworth, J. A.; Htoon, H.; Crooker, S. A.; Klimov, V. I. Breakdown of Volume Scaling in Auger Recombination in CdSe/CdS Heteronanocrystals: The Role of the Core-Shell Interface. *Nano Lett.* **2011**, *11* (2), 687−693.

(23) Bae, W. K.; Padilha, L. A.; Park, Y.-S.; McDaniel, H.; Robel, I.; Pietryga, J. M.; Klimov, V. I. Controlled Alloying of the Core-Shell Interface in CdSe/CdS Quantum Dots for Suppression of Auger Recombination. *ACS Nano* **2013**, *7* (4), 3411−3419.

(24) Boldt, K.; Kirkwood, N.; Beane, G. A.; Mulvaney, P. Synthesis of Highly Luminescent and Photo-Stable, Graded Shell CdSe/Cd X Zn 1− X S Nanoparticles by In Situ Alloying. *Chem. Mater.* **2013**, *25* (23), 4731−4738.

(25) Maiti, S.; Debnath, T.; Maity, P.; Ghosh, H. N. Tuning the Charge Carrier Dynamics via Interfacial Alloying in Core/Shell CdTe/ZnSe NCs. *J. Phys. Chem. C* **2016**, *120* (3), 1918−1925.

(26) Tschirner, N.; Lange, H.; Schliwa, A.; Biermann, A.; Thomsen, C.; Lambert, K.; Gomes, R.; Hens, Z. Interfacial Alloying in CdSe/CdS Heteronanocrystals: A Raman Spectroscopy Analysis. *Chem. Mater.* **2012**, *24* (2), 311−318.

(27) Dzhagan, V. M.; Valakh, M. Y.; Milekhin, A. G.; Yeryukov, N. A.; Zahn, D. R. T.; Cassette, E.; Pons, T.; Dubertret, B. Raman- and IR-Active Phonons in CdSe/CdS Core/Shell Nanocrystals in the Presence of Interface Alloying and Strain. *J. Phys. Chem. C* **2013**, *117* (35), 18225−18233.

(28) Todescato, F.; Minotto, A.; Signorini, R.; Jasieniak, J. J.; Bozio, R. Investigation into the Heterostructure Interface of CdSe-Based Core−Shell Quantum Dots Using Surface-Enhanced Raman Spectroscopy. *ACS Nano* **2013**, *7* (8), 6649−6657.

(29) McBride, J. R.; Kippeny, T. C.; Pennycook, S. J.; Rosenthal, S. J. Aberration-Corrected Z-Contrast Scanning Transmission Electron Microscopy of CdSe Nanocrystals. *Nano Lett.* **2004**, *4* (7), 1279−1283.

(30) Rosenthal, S. J.; McBride, J.; Pennycook, S. J.; Feldman, L. C. Synthesis, Surface Studies, Composition and Structural Characterization of CdSe, Core/Shell, and Biologically Active Nanocrystals. *Surf. Sci. Rep.* **2007**, *62* (4), 111−157.

(31) Abel, K. A.; Boyer, J.-C.; Andrei, C. M.; van Veggel, F. C. J. M. Analysis of the Shell Thickness Distribution on NaYF 4 /NaGdF 4 Core/Shell Nanocrystals by EELS and EDS. *J. Phys. Chem. Lett.* **2011**, *2* (3), 185−189.

(32) Midgley, P. A.; Weyland, M. 3D Electron Microscopy in the Physical Sciences: The Development of Z-Contrast and EFTEM Tomography. *Ultramicroscopy* **2003**, *96* (3−4), 413−431.

(33) Bals, S.; Casavola, M.; van Huis, M. A.; Van Aert, S.; Batenburg, K. J.; Van Tendeloo, G.; Vanmaekelbergh, D. Three-Dimensional Atomic Imaging of Colloidal Core-Shell Nanocrystals. *Nano Lett.* **2011**, *11* (8), 3420−3424.

(34) Van Aert, S.; Batenburg, K. J.; Rossell, M. D.; Erni, R.; Van Tendeloo, G. Three-Dimensional Atomic Imaging of Crystalline Nanoparticles. *Nature* **2011**, *470* (7334), 374−377.

(35) Kim, S. Y.; Jeong, J. S.; Mkhoyan, K. A.; Jang, H. S. Direct Observation of the Core/double-Shell Architecture of Intense Dual-Mode Luminescent Tetragonal Bipyramidal Nanophosphors. *Nanoscale* **2016**, *8* (19), 10049−10058.

(36) Lauhon, L. J.; Gudiksen, M. S.; Wang, D.; Lieber, C. M. Epitaxial Core−shell and Core−multishell Nanowire Heterostructures. *Nature* **2002**, *420* (6911), 57−61.

(37) Gan, L.; Heggen, M.; Rudi, S.; Strasser, P. Core-Shell Compositional Fine Structures of Dealloyed Pt xNi 1-X Nanoparticles and Their Impact on Oxygen Reduction Catalysis. *Nano Lett.* **2012**, *12* (10), 5423−5430.

(38) Hadar, I.; Philbin, J. P.; Panfil, Y. E.; Neyshtadt, S.; Lieberman, I.; Eshet, H.; Lazar, S.; Rabani, E.; Banin, U. Semiconductor Seeded Nanorods with Graded Composition Exhibiting High Quantum-Yield, High Polarization, and Minimal Blinking. *Nano Lett.* **2017**, *17* (4), 2524−2531.

(39) Yalcin, A. O.; Goris, B.; van Dijk-Moes, R. J. a; Fan, Z.; Erdamar, A. K.; Tichelaar, F. D.; Vlugt, T. J. H.; Van Tendeloo, G.; Bals, S.; Vanmaekelbergh, D.; Zandbergen, H. W.; van Huis, M. a. Heat-Induced Transformation of CdSe-CdS-ZnS Core-Multishell Quantum Dots by Zn Diffusion into Inner Layers. *Chem. Commun. (Cambridge, U. K.)* **2015**, *51* (16), 3320−3323.

(40) Peng, Z. A.; Peng, X. Formation of High-Quality CdTe, CdSe, and CdS Nanocrystals Using CdO as Precursor. *J. Am. Chem. Soc.* **2001**, *123* (1), 183−184.

(41) Thimsen, E.; Johnson, M.; Zhang, X.; Wagner, A. J.; Mkhoyan, K. A.; Kortshagen, U. R.; Aydil, E. S. High Electron Mobility in Thin Films Formed via Supersonic Impact Deposition of Nanocrystals Synthesized in Nonthermal Plasmas. *Nat. Commun.* **2014**, *5*, 5822.

(42) Odlyzko, M. L.; Held, J. T.; Mkhoyan, K. A. Atomic Bonding Effects in Annular Dark Field Scanning Transmission Electron

Microscopy. II. Experiments. *J. Vac. Sci. Technol., A* **2016**, *34* (4), 41603.

(43) Jeong, J. S.; Odlyzko, M. L.; Xu, P.; Jalan, B.; Mkhoyan, K. A. Probing Core-Electron Orbitals by Scanning Transmission Electron Microscopy and Measuring the Delocalization of Core-Level Excitations. *Phys. Rev. B: Condens. Matter Mater. Phys.* **2016**, *93* (16), 165140.

(44) LeBeau, J. M.; Findlay, S. D.; Allen, L. J.; Stemmer, S. Quantitative Atomic Resolution Scanning Transmission Electron Microscopy. *Phys. Rev. Lett.* **2008**, *100* (20), 206101.

(45) LeBeau, J. M.; Findlay, S. D.; Wang, X.; Jacobson, A. J.; Allen, L. J.; Stemmer, S. High-Angle Scattering of Fast Electrons from Crystals Containing Heavy Elements: Simulation and Experiment. *Phys. Rev. B: Condens. Matter Mater. Phys.* **2009**, *79* (21), 214110.

(46) Kirkland, E. J. *Advanced Computing in Electron Microscopy*, 2nd ed.; Springer Science & Business Media, 2010.

(47) Nelder, J. A.; Mead, R. A Simplex Method for Function Minimization. *Comput. J.* **1965**, *7* (4), 308−313.

(48) Hubbel, J. H.; Seltzer, S. M. *Tables of X-Ray Mass Attenuation Coefficients and Mass Energy-Absorption Coefficients*, version 1.4; National Institute of Standards and Technology: Gaithersburg, MD, 2004. Available at https://www.nist.gov/pml/x-Ray-Mass-Attenuation-Coefficients (accessed Nov 3, 2017).

(49) Kirkland, E. J.; Loane, R. F.; Silcox, J. Simulation of Annular Dark Field Stem Images Using a Modified Multislice Method. *Ultramicroscopy* **1987**, *23* (1), 77−96.

(50) Pennycook, S. J. Z-Contrast Stem for Materials Science. *Ultramicroscopy* **1989**, *30* (1−2), 58−69.

(51) Wang, Z. W.; Li, Z. Y.; Park, S. J.; Abdela, A.; Tang, D.; Palmer, R. E. Quantitative Z-Contrast Imaging in the Scanning Transmission Electron Microscope with Size-Selected Clusters. *Phys. Rev. B: Condens. Matter Mater. Phys.* **2011**, *84* (7), 73408.